Available online at www.sciencedirect.com

SciVerse ScienceDirect

Acta Materialia 61 (2013) 2909–2918

Acta MATERIALIA

www.elsevier.com/locate/actamat

Phase field simulations of ferroelectrics domain structures in $PbZr_xTi_{1-x}O_3$ bilayers

F. Xue [a,*], J.J. Wang [a,b], G. Sheng [a], Esther Huang [c], Y. Cao [a], H.H. Huang [c], Paul Munroe [c], R. Mahjoub [c], Y.L. Li [d], Valanoor Nagarajan [c], L.Q. Chen [a]

[a] Department of Materials and Engineering, Pennsylvania State University, University Park, PA 16802, USA
[b] Department of Physics, University of Science and Technology Beijing, Beijing 100083, China
[c] School of Materials Science and Engineering, University of New South Wales, Sydney, NSW 2052, Australia
[d] Pacific Northwest National Laboratory, Richland, WA 99354, USA

Received 21 October 2012; received in revised form 18 January 2013; accepted 20 January 2013
Available online 1 March 2013

Abstract

Domain stability and structures in $Pb(Zr_{0.3}Ti_{0.7})O_3/Pb(Zr_{0.7}Ti_{0.3})O_3$ bilayer films under different substrate strains are studied using the phase field method. It is demonstrated that the domain structure of the bilayer film is very different from those of the corresponding single layer films grown on the same silicon substrate with an incoherent interface. Moreover, the predicted rhombohedral domains in the $Pb(Zr_{0.7}Ti_{0.3})O_3$ layer of the bilayer film have smaller sizes than those in the single layer case. These results are compared with experimental observations and previous thermodynamic analyses. The polarization distributions of the ferroelectric–paraelectric bilayer are analyzed as a function of the thickness of the bilayer film, where there is a "ferroelectric proximity effect" due to dipole–dipole interactions. The phase diagrams for both the bilayer and single layer films as a function of temperature and effective in-plane substrate strain are constructed.

Keywords: Ferroelectric; Bilayer; Domain structures; Phase field simulations

1. Introduction

Multilayered heterostructures with unique functional properties have attracted significant attention. The properties of such multilayered systems can be tuned through control of the composition, the thickness of each layer, and the number of alternating layers [1–3]. For example, it has been shown that multilayered ferroelectric thin films demonstrate both pronounced polarization and high dielectric permittivity compared with single layer films [4–8]. Many factors can lead to these enhanced properties, including electric field-induced coupling [1], morphotropic phase boundary effects [5], epitaxial strains [8–10], and unique electrostatic interactions between the two layers [4,11]. Recently, piezoresponse force microscopy (PFM) and cross-sectional transmission electron microscopy (TEM) analyses revealed a unique "herringbone" ferroelastic domain structure in $PbZr_{0.3}Ti_{0.7}O_3/PbZr_{0.7}Ti_{0.3}O_3$ bilayers. The ferroelastic domains were shown to be mobile under an applied external electric field, leading to an electromechanical coefficient up to three times larger than that in constrained single layered $PbZr_{0.3}Ti_{0.7}O_3$ thin films [12]. These results were supported by a thermodynamic theory which found that the out-of-plane piezoelectric coefficients d_{33} in bilayers can be an order of magnitude larger than the corresponding single layer constituents due to electrical and electromechanical interdomain and interlayer interactions [13].

A number of theoretical investigations of the domain stabilities and ferroelectric properties of multilayered heterostructured thin films [11,12,14–16] have discussed

* Corresponding author. Tel.: +1 8149542056.
E-mail address: xuefei5376@gmail.com (F. Xue).

1359-6454/$36.00
http://dx.doi.org/10.1016/j.actamat.2013.01.038

the critical role of electrostatic interactions in the electromechanical response of ferroelectric multilayers. Recently phase field simulations have been applied to understand domain structure evolution during the ferroelectric transition [17], including bulk single crystals [18–20] and confined nanoferroelectrics [21]. Li et al. [22] extended the model by incorporating the elastic solution for thin films in an elastically anisotropic system combining Khachaturyan's microscopic elasticity theory [23,24] and Stroh's formalism of anisotropic elasticity [25,26]. This thin film model has been successfully applied to predicting the domain structures in a number of constrained three-dimensional (3-D) ferroelectric thin film systems [27–29]. In particular, the phase field model was applied to a barium titanate–strontium titanate (BT–ST) superlattice based on the bulk model with various coefficients and properties along the thickness direction. Results from simulations of the dependence of the phase transition temperature on the number of perovskite unit cells along the growth direction of each layer showed quantitative agreement with ultraviolet Raman spectroscopy, and the polarization distribution across the superlattice thickness was calculated under different interfacial coherencies in the superlattice simulation using the phase field model [30,31].

In this work the phase field method is extended to study the domain structure in a PZT bilayer system with differing compositions in the two layers. We studied the strain effect in each individual layer and electrostatic interaction between the two layers on the domain structures. These were compared with the single layer case for the same composition and thickness. We finally constructed strain–temperature phase diagrams for the bilayer system and compared them with the single layer film diagram. These results were also compared with experimental observations and prior thermodynamic analyses. It was found that mechanical and electrostatic interactions between the two layers may lead to significantly different domain structures from the single layer, resulting in fundamentally different physical properties from the individual layer systems.

2. Framework of the phase field model

We consider a ferroelectric bilayer system which comprises two layers with different compositions. Fig. 1 shows a schematic plot of the bilayer system, wherein the z-axis represents the out-of-plane direction. The bottom layer is (001) $Pb(Zr_{0.7}Ti_{0.3})O_3$ (R), while the top layer is (001) $Pb(Zr_{0.3}Ti_{0.7})O_3$ (T). In the phase field model temporal evolution of the polarization vector field is described by the time-dependent Ginzburg–Landau equations, i.e.

$$\frac{\partial P_i(\vec{r},t)}{\partial t} = -L\frac{\delta F}{\delta P_i(\vec{r},t)}, \quad (i=1,2,3) \tag{1}$$

where L is the kinetic coefficient related to the domain wall mobility. The total free energy in Eq. (1) includes the bulk free energy, elastic energy, electrostatic energy, and gradient energy [32,33], i.e.

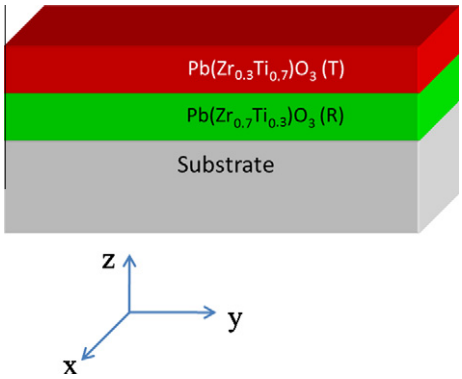

Fig. 1. Schematic plot of a PZT bi-layer thin film.

$$F = \int_V [f_{\text{bulk}} + f_{\text{elas}} + f_{\text{elec}} + f_{\text{grad}}]dV \tag{2}$$

where V is the system volume of the bilayer, f_{bulk} denotes the bulk free energy density, f_{elas} the elastic energy density, f_{elec} the electrostatic energy density and f_{grad} the gradient energy density.

The bulk free energy density in each layer is expanded in terms of polarization components P_i using the Landau theory, i.e.

$$\begin{aligned} f_{\text{bulk}} = {} & \alpha_1(P_1^2+P_2^2+P_3^2) + \alpha_{11}(P_1^4+P_2^4+P_3^4) \\ & + \alpha_{12}(P_2^2P_3^2+P_1^2P_2^2+P_1^2P_3^2) + \alpha_{111}(P_1^6+P_2^6 \\ & + P_3^6) + \alpha_{112}[P_1^4(P_2^2+P_3^2)+P_2^4(P_1^2+P_3^2) \\ & + P_3^4(P_1^2+P_2^2)] + \alpha_{123}P_1^2P_2^2P_3^2 \end{aligned} \tag{3}$$

where the coefficients α_i, α_{ij}, and α_{ijk} are fitted using the physical properties and phase transitions of a ferroelectric under stress-free boundary conditions. It should be noted that the first coefficient is related to the relative dielectric permittivity of the material by the expression: $\alpha_1 = 1/2\omega_0\chi = 1/2\omega_0(\kappa_{ii}-1)$, where ω_0 is the dielectric permittivity of a vacuum, χ is the susceptibility of the material, and κ_{ii} is the relative dielectric permittivity.

The gradient energy comes from the domain wall and can be described by the gradients of the polarization field. For simplicity it is assumed that the gradient energy is isotropic, and the gradient energy density is written as:

$$\begin{aligned} f_{\text{grad}} = {} & \frac{1}{2}G_{11}(P_{1,1}^2+P_{2,2}^2+P_{3,3}^2) + G_{12}(P_{1,1}P_{2,2} \\ & + P_{2,2}P_{3,3}+P_{1,1}P_{3,3}) + \frac{1}{2}G_{44}[(P_{1,2}+P_{2,1})^2 \\ & + (P_{2,3}+P_{3,2})^2 + (P_{1,3}+P_{3,1})^2] + \frac{1}{2}G'_{44}[(P_{1,2} \\ & + P_{2,1})^2 + (P_{2,3}+P_{3,2})^2 + (P_{1,3}+P_{3,1})^2] \end{aligned} \tag{4}$$

where G_{11}, G_{12}, G_{44}, and G'_{44} are the gradient energy coefficients and the comma in the subscript represents spatial differentiation, i.e. $P_{i,j} = \partial P_i/\partial x_j$.

The elastic energy can be written as:

$$f_{\text{elas}} = \frac{1}{2}c_{ijkl}e_{ij}e_{kl} = \frac{1}{2}c_{ijkl}(\varepsilon_{ij}-\varepsilon_{ij}^0)(\varepsilon_{kl}-\varepsilon_{kl}^0) \tag{5}$$

where c_{ijkl} is the elastic stiffness tensor, e_{ij} is the elastic strain and ε^0_{kl} is the stress-free strain. The summation convention for the repeated indices is employed, and the letters i, j, k, l are taken as 1, 2, 3 in this paper. The total strain ε_{ij} in Eq. (5) is given as:

$$\varepsilon_{ij} = \bar{\varepsilon}_{ij} + \eta_{ij} \tag{6}$$

where $\bar{\varepsilon}_{ij}$ is the homogeneous strain and η_{ij} is the heterogeneous strain which satisfies the condition $\int_V \eta_{ij} dV = 0$. If $\bar{\varepsilon}_{\alpha\beta}(\alpha, \beta = 1, 2)$ represent the macroscopic shape deformation of the film in the film plane then:

$$\bar{\varepsilon}_{11} = \bar{\varepsilon}_{22} = \frac{a_{\text{final}} - a_{\text{ref}}}{a_{\text{ref}}}, \quad \bar{\varepsilon}_{12} = \bar{\varepsilon}_{21} = 0 \tag{7}$$

where a_{ref} is the reference lattice parameter before deformation and a_{final} is the final lattice parameter due to substrate-induced deformation. Therefore, $\bar{\varepsilon}_{\alpha\beta}$ is the misfit strain between the thin film and the substrate. The heterogeneous strain can be obtained by the space differential of displacement u_i, i.e.

$$\eta_{ij} = \frac{1}{2}(u_{i,j} + u_{j,i}) \tag{8}$$

For a bilayer system the total stress-free strain consists of two contributions, the ferroelectric transition and the lattice mismatch with respect to the reference lattice parameter, i.e. $\varepsilon^0_{ij} = Q_{ijkl} P_k P_l + \varepsilon^{\text{latt}}_{ij}$, where Q_{ijkl} represents the electrostrictive coefficient, and $\varepsilon^{\text{latt}}_{ij}$ is the mismatch strain caused by lattice parameter differences between the two layers. The lattice mismatch strain of the top layer can be written as:

$$\varepsilon^{\text{latt}}_{ij}(\text{top}) = \frac{a_{\text{top}} - a_{\text{ref}}}{a_{\text{ref}}} \tag{9}$$

where a_{top} is the lattice parameter of the top layer. And the lattice mismatch strain in the bottom layer is given by:

$$\varepsilon^{\text{latt}}_{ij}(\text{bott}) = \frac{a_{\text{bott}} - a_{\text{ref}}}{a_{\text{ref}}} \tag{10}$$

where a_{bott} is the lattice parameter of the bottom layer.

In linear elasticity the stress σ_{ij} is related to the elastic strain e_{ij} by Hooke's law:

$$\sigma_{ij} = c_{ijkl} e_{kl} = c_{ijkl}(\varepsilon_{kl} - \varepsilon^0_{kl}) \tag{11}$$

and the mechanical equilibrium equations $\sigma_{ij,j} = 0$ should be satisfied inside the bilayer system, including both the film and the substrate. It is assumed that the thin film has a stress-free top surface and the substrate is fixed in a region far from the interface between the film and the substrate.

For a cubic structure the system has three independent elastic constants C_{11}, C_{12} and C_{44} in Voigt's notation. The elastic energy can be rewritten as:

$$f_{\text{elas}} = \frac{1}{2} C_{11}(e^2_{11} + e^2_{22} + e^2_{33}) + C_{12}(e_{11}e_{22} + e_{22}e_{33} + e_{11}e_{33}) + 2C_{44}(e^2_{12} + e^2_{23} + e^2_{13}) \tag{12}$$

The electrostatic energy in the bilayer without an externally applied electric field is given by

$$f_{\text{elec}} = -\frac{1}{2} E_i P_i \tag{13}$$

where the electric field $E_i = -\varphi_{,i}$ and φ is the electrostatic potential. The electrostatic equilibrium equation is given by:

$$\kappa^b_{ii} \omega_0 \varphi_{ii} = P_{i,i} \tag{14}$$

where κ^b_{ii} is the background dielectric constant [34–37]. In our simulations a short-circuit electric boundary condition is employed. Details about how to solve the electrostatic equilibrium equations, as well as the mechanical equilibrium equations, can be found in Li et al. [22,38].

3. Modeling the interactions of two layers

The variation in the composition-dependent coefficient ζ within the bilayer is described as follows:

$$\zeta = \zeta_{\text{top}} + \varphi(\zeta_{\text{bott}} - \zeta_{\text{top}}) \tag{15}$$

where ζ_{top} and ζ_{bott} represent the Landau coefficients or electrostrictive coefficients of the top and bottom layers, respectively, and φ takes the value of 0.0 in the top layer and 1.0 in the bottom layer. In order to solve the electrostatic equilibrium equations and the mechanical equilibrium equations for the entire bilayer the elastic coefficients and dielectric permittivity are assumed to be independent of the composition, i.e. the elastic stiffness modulus and the background dielectric constant κ^b_{ii} are assumed to be the same for the top and bottom layers. Then the electrostatic and ferroelastic interactions between the two layers are considered spontaneously.

Assuming the thicknesses of the two layers are h_T and h_R, respectively, then the reference lattice parameter a_{ref} can be given by

$$a_{\text{ref}} = \frac{a_T h_T + a_R h_R}{h_T + h_R} \tag{16}$$

If the two layers are coherent the two layers will both end up with a_{ref} after annealing at high temperature.

4. Numerical simulations

In this work the semi-implicit Fourier spectral method for both time stepping and spatial discretization is employed to solve Eq. (1) [39]. The initial film is in a paraelectric state, which was created by assigning a value of 0 to each component of polarization at each lattice site plus a small amount of random noise. Here we take a ferroelectric bilayer consisting of a T layer and a R layer of the same thickness, 20.0 nm. The pseudocubic lattice parameters of the T layer and the R layer are 4.0185 and 4.1032 Å, respectively. These parameters were calculated using the interpolation of available parameters for various $PbTiO_3$ and PZT compositions given in Haun et al. [40,41] and Khaenamkaew et al. [42], then the reference lattice parameter $a_{\text{ref}} = (4.1032 + 4.0185)/2 = 4.0609$ Å. The mismatch strains caused by a lattice parameter difference between

the two layers are $\varepsilon_{ii}^{\text{latt}}(T) = -1.04\%$ and $\varepsilon_{ii}^{\text{latt}}(R) = 1.04\%$, respectively.

The Landau coefficients and electrostrictive coefficients are from Haun et al. [40,41,43] and the elastic constants are set as $C_{11} = 1.696 \times 10^{11}$, $C_{12} = 8.187 \times 10^{10}$ and $C_{44} = 4.717 \times 10^{10}$ N m^{-2} [44]. We employed $128 \times 128 \times 40$ discrete points for the bilayer film and $128 \times 128 \times 12$ points for the substrate. The periodic boundary conditions were applied along the x and y directions. The grid spaces in real space are the same along the three directions, i.e. $\Delta x/l_0 = \Delta y/l_0 = \Delta z/l_0 = 1.0$, where $l_0 = 1.0$ nm. We set the gradient energy coefficients as $G_{11}/G_{110} = 0.6$, $G_{12}/G_{110} = 0.0$, $G_{44}/G_{110} = G'_{44}/G_{110} = 0.3$, where $G_{110} = 1.73 \times 10^{-10}$ C^{-2} m^4 N [22].

5. Results

5.1. Domain structures in a PZT bilayer and single layer

We first studied the domain configurations of a PZT bilayer film grown on a silicon substrate at room temperature, 25 °C, as a specific example. It is assumed that the bilayer system is incoherent with the substrate and the strain for the bilayer film with the substrate is 0.2% due to the different thermal expansion coefficients of the film and substrate. The in-plane lattice parameter of (0 0 1) silicon is 3.840 Å, while the bottom R layer has a quasi-cubic lattice parameter of 4.1032 Å. If the bilayer system is coherent with the substrate the in-plane strain of the R layer would be 6.41%, which is too large for a conventional PZT thin film (the typical strain range is from −2.00% to 2.00%). Therefore, the bilayer was assumed to be incoherent with the substrate. The substrate strain is relaxed through interfacial dislocations and these interfacial dislocations can modify the ferroelectric phase transition temperature and remnant polarization based on our earlier work [45,46]. In this paper, however, for simplicity the effect of dislocations is ignored.

If zero substrate strain is imposed on the bilayer film the domain structure does not change significantly from the simulation results, which indicates that the 0.2% substrate strain has only a minor influence on the domain configurations in this case. We discuss data when different substrate strains are applied to the bilayer later in Section 6.3.

Fig. 2a shows the domain structures of this bilayer system when the T layer and R layer are coherent with each other. The domain variants are represented by different colors and the arrows indicate the directions of the polarization vectors. The top layer is mainly composed of a tetragonal a_1/a_2 twin domain structure with polarization vectors along the [1 0 0] or [0 1 0] direction, while the bottom layer exhibits tetragonal c domains with out-of-plane polarization. On the other hand, if the single layer film is deposited on the Si substrate and the same substrate strain, 0.2%, is imposed the domain structure consists of c/a/c/a domains in the T layer film and rhombohedral domains in the R layer film, as shown in Fig. 2c and d.

These differences (between the corresponding layers in the coherent bilayer film and the individual layer films) on domain morphologies can be explained in terms of misfit strain caused by the lattice differences between the two layers. It is worth noting that the misfit strain here refers to $\varepsilon_{ij}^{\text{latt}}$, part of the stress-free strain, as shown in Eqs. (9) and (10), unlike the conventional meaning of "misfit strain". When the average of the lattice parameters of the two layers is chosen as a reference the misfit strain of the top layer is −1.04% and the substrate strain is 0.2%, caused by thermal expansion. However, with respect to the lattice parameter of the top layer itself, the top layer is under a tensile in-plane substrate strain of 1.24%. We can define the effective in-plane strain as the substrate strain minus the misfit strain, i.e.

$$\varepsilon_{eff} = \varepsilon_{sub} - \varepsilon_{latt} \tag{17}$$

Table 1 lists the misfit strain, in-plane substrate strain, and effective in-plane strain of each layer in the bilayer film when a different reference lattice parameter is chosen. It shows that the effective in-plane strain is independent of the reference lattice parameter, and thus can be used to characterize the strain distribution. The effective in-plane strain of the top layer is 1.24% and the effective in-plane strain of the bottom layer is −0.84%. We examined the domain structures of single layers under the same strains. Fig. 3a shows that a $Pb(Zr_{0.3}Ti_{0.7})O_3$ film under a substrate strain of 1.24% consists of a_1/a_2 domains, while a $Pb(Zr_{0.7}Ti_{0.3})O_3$ film exhibits tetragonal c domains under a substrate strain of −0.84% (Fig. 3b). Therefore, the effective in-plane strain largely determines the final domain structures in each separate layer.

From Eqs. (5) and (6), we can obtain the elastic strain:

$$\begin{aligned} e_{ij} &= \varepsilon_{ij} - \varepsilon_{ij}^0 = \bar{\varepsilon}_{ij} + \eta_{ij} - \left(Q_{ijkl}P_kP_l + \varepsilon_{ij}^{\text{latt}}\right) \\ &= \left(\bar{\varepsilon}_{ij} - \varepsilon_{ij}^{\text{latt}}\right) + \eta_{ij} - Q_{ijkl}P_kP_l \\ &= \varepsilon_{\text{eff}} + \eta_{ij} - Q_{ijkl}P_kP_l \end{aligned} \tag{18}$$

Compared with the expression for the elastic strain of the single layer [22], the effective in-plane strain of the bilayer has the same effect on the domain structures as the substrate strain in the single layer case.

Fig. 2b shows the domain structures when the two layers are incoherent. Both the T and R layers are only under the effect of a substrate strain of 0.2%. The top T layer shows c/a domains, while the bottom R layer shows rhombohedral domains. However, it should be noted that, as circled in Fig. 2b, due to ferroelastic and electrostatic interactions between the two layers some tetragonal domains expand into the R layer, and vice versa. These parts may be very sensitive to external stimuli, e.g. an electric field, and can produce an enhanced electromechanical response. This may be one reason why the bilayer film shows a larger piezoelectric coefficient than a single layer [12,47].

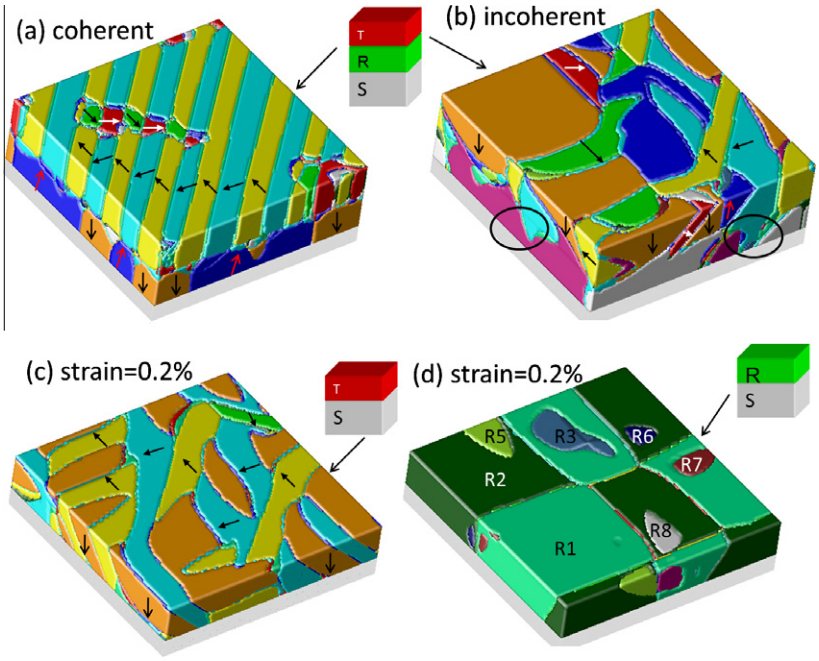

Fig. 2. (a) and (b) Domain structures of a PZT bi-layer film when (a) the two layers are coherent and (b) the two layers are incoherent. (c) and (d) Domain structures of a single layer under different strain conditions: (c) a single T layer under tensile substrate strain 0.2%; (d) a single R layer under tensile substrate strain 0.2%.

Table 1
Misfit strain, substrate strain and effective in-plane strain in different references.

	Misfit strain (%)	Substrate strain (%)	Effective in-plane strain (%)
Top layer (taking the average as reference)	−1.04	0.20	1.24
Top layer (taking the top layer as reference)	0.00	1.24	1.24
Bottom layer (taking the average as reference)	1.04	0.20	−0.84
Bottom layer (taking the bottom layer as reference)	0.00	−0.84	−0.84

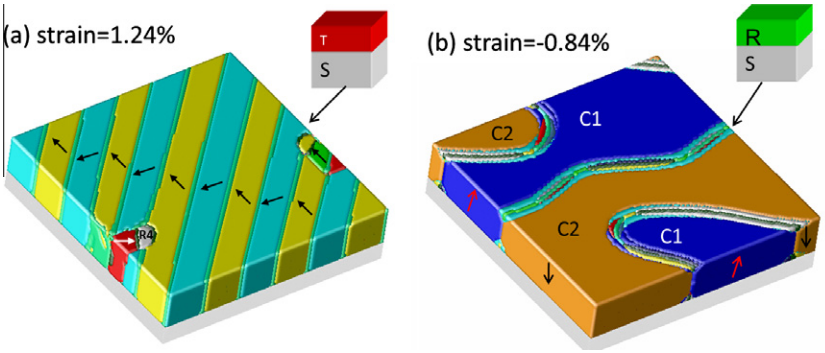

Fig. 3. Domain structures of a single layer under different strain conditions: (a) a single T layer under tensile substrate strain 1.24%; (b) a single R layer under compressive substrate strain -0.84%.

5.2. The domain size differences of single layers and the bilayer

In this section we will demonstrate the rhombohedral domain size differences between the bilayer system when the two layers are coherent and a single layer under the same effective in-plane strain. Fig. 4a and c shows the domain structures of the bottom layer of the bilayer constrained by effective in-plane strains of 0.20% and −1.0%, respectively. As expected, rhombohedral domains and tetragonal c domains are formed in Fig. 4a and c, respectively. The domain structures of the single layers under substrate strains of 0.20% and −1.0% are shown in Fig. 4b and d, respectively. It can be seen that Fig. 4a and c shows much smaller (about half the size) domains than those shown in Fig. 4b and d. This should be due to the impact of polarization of the top

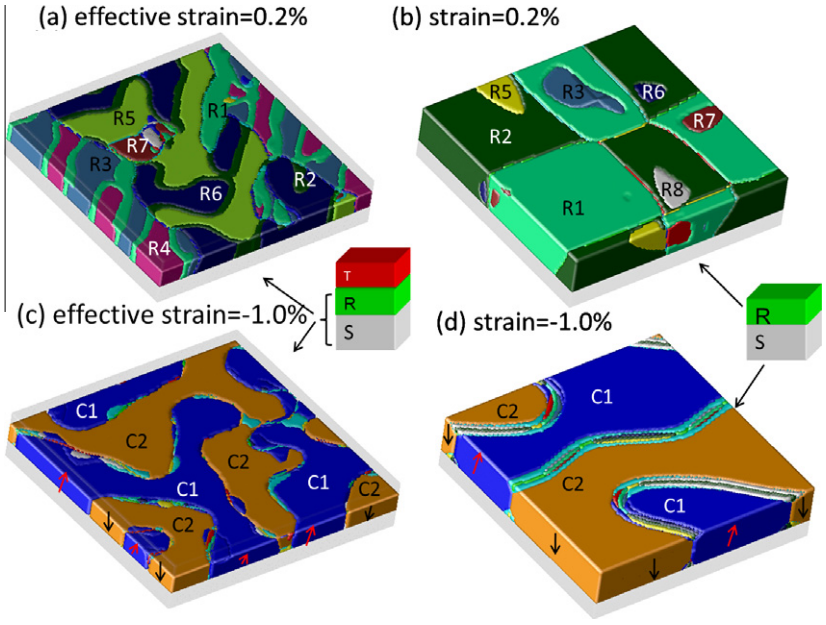

Fig. 4. Domain configurations of the R layer in a bi-layer system and a single layer of the same composition: (a) the R layer of the bi-layer under effective in-plane strain 0.2%; (b) a single R layer under substrate strain 0.2%; (c) the R layer of the bi-layer under effective in-plane strain -1.0%; (d) a single R layer under substrate strain -1.0%.

layer. In our simulations numbers of small domains are first formed, which then evolve into bigger domains, specifically a domain "coarsening process". In the case of a single layer the coarsening process continues until the energy barrier forbids the domains becoming even larger. However, for the bilayer system the domains in the R layer are required to be compatible with not only the neighboring domains in the R layer, but also the domains in the top T layer. If the domains in the R layer disappear or grow, the domains in the T layer must change correspondingly. Therefore, the domain coarsening process in the bilayer confronts a higher energy barrier and ceases earlier, resulting in a smaller domain size compared with the single layer.

6. Discussion

6.1. Interactions between the two layers and comparison with experiments

As shown in Section 5.1, when the two layers are coherent the misfit strain between the two layers plays a critical role in determining the domain structures. We also performed simulations for $Pb(Zr_{0.3}Ti_{0.7})O_3$ (T)/$Pb(Zr_{0.55}Ti_{0.45})O_3$ (R) bilayers and obtained similar domain structures, shown in Fig. 2a, when the two layers are coherent and incoherent with the substrate. Based on the simulation results and analysis we can make the following predictions.

i. If the thickness of both the layers is less than 30 nm we can assume that the two layers are coherent. If these two layers are coherent with the substrate (such as $SrTiO_3$) the strain condition of the bilayer will be determined by the substrate.
ii. If the thickness of the two layers is less than 30 nm and the two layers are coherent with each other but the bilayer is not coherent with the substrate the final pseudo-cubic lattice parameter is the average of the pseudo-cubic lattice parameters of the two layers. The T layer is under a tensile strain from the R layer and shows a_1/a_2 domains, while the R layer is under a compressive strain from the T layer and shows tetragonal c domains, as shown in Fig. 2a.
iii. If the bottom R layer is thick (i.e. a thickness greater than 70 nm) while the T layer has a thickness of less than 30 nm we can assume that the strain from the substrate is relaxed and the R layer is incoherent with the substrate, while the T layer is coherent with the R layer. In this case the T layer is under a tensile strain from the R layer and should show a_1/a_2 domains.
iv. If both the T and R layers are thick (greater than 70 nm) it can be assumed that the two layers are incoherent with each other. The T layer will show c/a/c/a domains, while the R layer will show rhombohedral domains, as shown in Fig. 2b.
v. It can thus be inferred that the bottom R layer acts as the controlling interface for the top T layer and produces a tensile strain on the T layer similar to the substrate. However, the interaction between the two layers is more than that. The R layer is a ferroelectric phase and there is a strong electrostatic interaction between the two layers. The electrostatic and ferroelastic interactions may lead to the presence of rhombohedral domains in the T layer and tetragonal domains in the R layer, which may result in an enhanced piezoelectric coefficient. These interactions may also cause a smaller

domain size in the R layer, compared with a single layer with the same composition and under the same strain conditions.

To test the validity of the model predictions two different $Pb(Zr_{0.3}Ti_{0.7})O_3$ (T)/$Pb(Zr_{0.55}Ti_{0.45})O_3$ (R) bilayer epitaxial thin film systems deposited on (0 0 1) $SrTiO_3$ were investigated. It should be noted that both films included a coherent layer of $(La_{0.67}Sr_{0.33})MnO_3$ as the bottom electrode. Fig. 5a is a bright field cross-sectional TEM image along the [0 0 1] zone axis for a bilayer where both layers are ~100 nm thick. We find that both interfaces (i.e. between the T and R layer and between the R layer and the substrate) are semi-coherent. The T layer shows the clear presence of c/a/c/a domains. The corresponding diffraction pattern is shown in Fig. 5b. The presence of distinct reflections (as opposed to rings and diffuse scattering) confirms the epitaxial quality of the sample. The diffraction pattern confirms the presence of c/a/c/a domains and is indexed accordingly. The average *c*-axis lattice parameter measured is 0.414 nm and the average *a*-axis parameter is 0.397 nm. These values are close to the expected bulk lattice parameters for this composition and hence confirm almost full relaxation of the elastic energy.

In contrast, the bright field cross-sectional TEM image for a 30 nm T layer deposited on a 100 nm R layer shows no presence of c/a/c/a domains, as shown in Fig. 6a. The corresponding diffraction pattern reveals an in-plane lattice constant of 0.411 nm and an out-of-plane lattice constant of 0.395 nm. The in-plane lattice parameter of the R layer in all cases was measured to be ~0.41 nm. In other words, the T layer is closely matched with the in-plane lattice parameter of the R layer. The tensile strain due to the R layer creates *a*-axis oriented domains in the film. We could

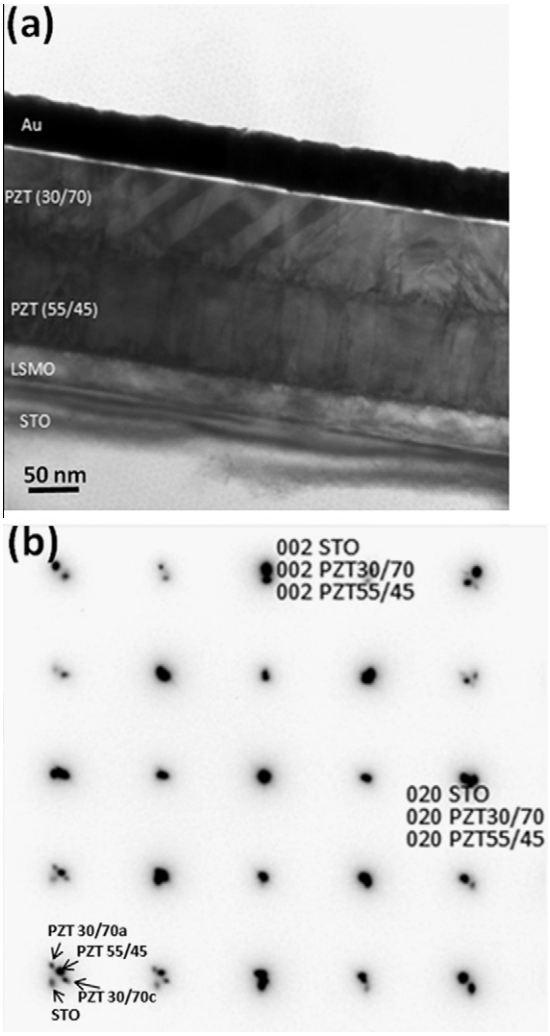

Fig. 5. (a) [100] cross-sectional bright-field TEM image for a thick PZT (30/70)/PZT (55/45)/LSMO/STO sample and (b) selected-area diffraction pattern taken from [100] zone axis of an area that includes the entire heterostructure. The set of 4 reflections at {220} positions is a clear indication of the polydomain structure.

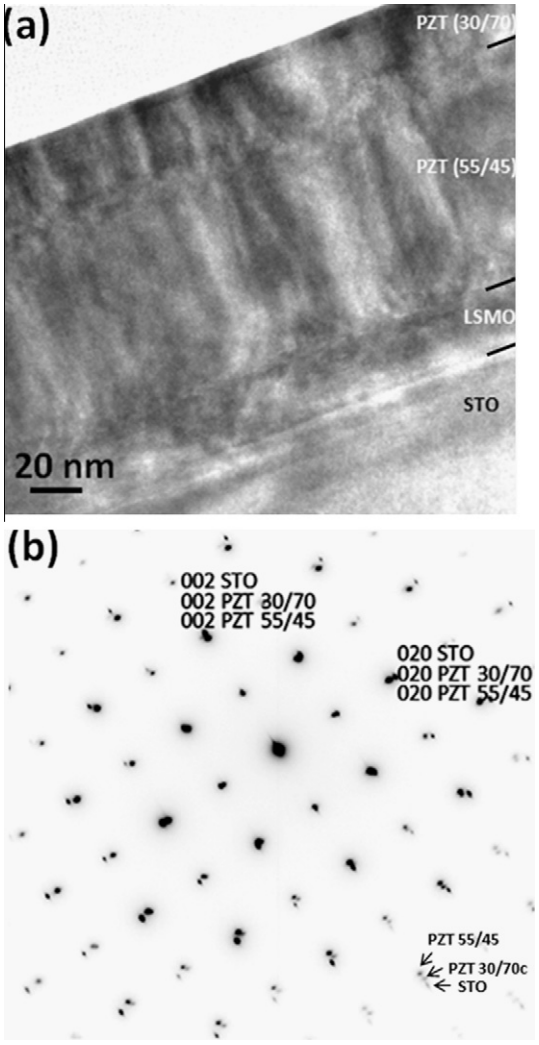

Fig. 6. (a) [100] cross-sectional bright-field TEM image for a thin PZT (30/70)/PZT (55/45)/LSMO/STO sample and (b) selected-area diffraction pattern taken from the [100] zone axis of an area that includes the entire heterostructure.

not observe a_1/a_2 domain walls, which may be due to the [0 0 1] zone axis used. Additionally, some local regions (~50 nm in size) were found to have fine c/a/c/a non-equilibrium domains, which could not be attributed to any thermodynamic driving forces. These most likely stem from point defects in the sample. Nevertheless, the experiments demonstrate the underpinning message of our model, i.e. the final phase in the T layer is primarily determined as a function of the interfacial strain imposed by the R layer and not significantly by the nature of the bottom substrate.

In earlier reported experiments the top T layer of the bilayer showed tetragonal herringbone c/a/c/a domains [12]. The appearance of c/a/c/a domains is due to the fact that the two layers are not coherent with each other since they are thick (each layer has a thickness of 70 nm), and X-ray diffraction data confirmed this [12]. Furthermore, here we propose a possible mechanism for the appearance of the herringbone ferroelastic domain structure. Anbusathaiah et al. claimed that they are $c/a_1/c/a_2$ domains. However, according to the domain wall orientations of Fig. 1e in Anbusathaiah et al. [12] it is more likely that they are $c^+/a_1/c^-/a_1$ domains. Our simulation above demonstrates that the $c^+/a_1/c^-/a_1$ domains are not directly caused by interactions between the two layers. One possible reason for the herringbone domains is mechanical interactions between neighboring grains in the top T layer. It has been shown that the $PbTiO_3$ film may exhibit $c^+/a_1/c^-/a_1$ domains under certain anisotropic misfit strains [29]. Therefore, if a grain in the T layer is anisotropically clamped by the neighboring grains it may show $c^+/a_1/c^-/a_1$ domains.

6.2. The "ferroelectric proximity" effect in ferroelectric–paraelectric bilayer

In this section we will investigate the polarization distribution of a ferroelectric–paraelectric bilayer under the assumption that the two layers are coherent. Since the Curie temperature in the bulk phase of the bottom R layer (334 °C) is lower than that of the top T layer (425 °C), the top T layer is ferroelectric, while the bottom R layer is paraelectric at 350 °C. Fig. 7 shows the average polarization components over the x–y plane as a function of distance from the substrate, i.e.

$$\overline{P_i}(h) = \frac{1}{128 \times 128} \sum_{m=1}^{128} \sum_{n=1}^{128} |P_i(m,n,h)| \tag{19}$$

where $i = x, y,$ or z, P_i is the ith component of polarization, (m,n,h) denote the coordinates of one grid in the bilayer, with m and n referring to the in-plane coordinates while h is the out-of-plane coordinate. It should be noted that the "strain" in the label of the four figures refers to the effective in-plane strain within each layer, and T_c refers to the Curie temperature of the R layer (334 °C). Fig. 7a shows that the lower half of the R layer is paraelectric at 350 °C under an effective in-plane strain of 0.00%. However, close to the T layer P_x and P_y increase while P_z remains small, and the domain structures smoothly change into a_1/a_2 domains. The T layer seems to be unaffected by the R layer, while the upper half of the R layer is significantly modified by the T layer. If we artificially switch off the dipole–dipole interactions and the gradient energy the induced polarization in the upper half of the R layer will disappear. Thus the polarization within the R layer is not the result of a ferroelectric phase transition, but rather is induced by the dipolar field produced by the T layer, i.e. a result of a "ferroelectric proximity" effect [11,48]. This is also observed in BT–ST superlattices [30,31].

It is known that a single layered film with the R layer composition under a compressive strain of 0.2% changes into tetragonal c domains at 350 °C [49]. For the bilayer case, when an effective in-plane strain of 0.2% is imposed on the R layer the lower half of the R layer also shows c domains (Fig. 7b). Close to the T layer the c domains slowly change to a_1/a_2 domains.

In order to make a comparison with the polarization distribution above the Curie temperature we also examined the average polarization at 310 °C, slightly below $T_c = 334$ °C. It is well known that polarization is reduced near the Curie temperature. In the bilayer case, as shown in Fig. 7c, in the lower half of the R layer the magnitudes of three polarization components are almost the same, indicating the rhombohedral phase. However, close to the T layer P_x and P_y increase in magnitude while P_z remains unchanged, indicating that the domain structures turns more slowly into a_1/a_2 domains. The effect of the T layer on the R layer is much larger than that of the R layer on the T layer. This is because the T layer is far below its Curie temperature, while for the R layer the temperature is slightly lower than its Curie temperature and the ferroelectric behavior near the Curie temperature is "softer". When an effective in-plane strain of 0.2% is imposed on the R layer the lower half of R the layer exhibits tetragonal c domains: $P_x = P_y \approx 0$ and $P_z > 0$, as shown in Fig. 7d. This means that compressive strain changes the R layer from rhombohedral phase to tetragonal c phase [39]. The polarization distribution is similar to that in Fig. 7b.

6.3. Phase diagrams

Finally, we obtained the phase diagrams of the T layer and R layer for both the bilayer and single layer films. Since the upper half of the R layer in the bilayer film is modified by the T layer, we classified its phase by analyzing the lower half of the R layer, and the result is presented in Fig. 8a. Similarly, the phases of the T layer were classified by examining the upper half of the T layer, and the phase diagram is given in Fig. 8b. It should be noted that the abscissa refers to the effective in-plane strain for the bilayer film and substrate strain for the single layer film. It can be seen from Fig. 8 that the phase boundaries of both layers shift only slightly under the impact of the other layer.

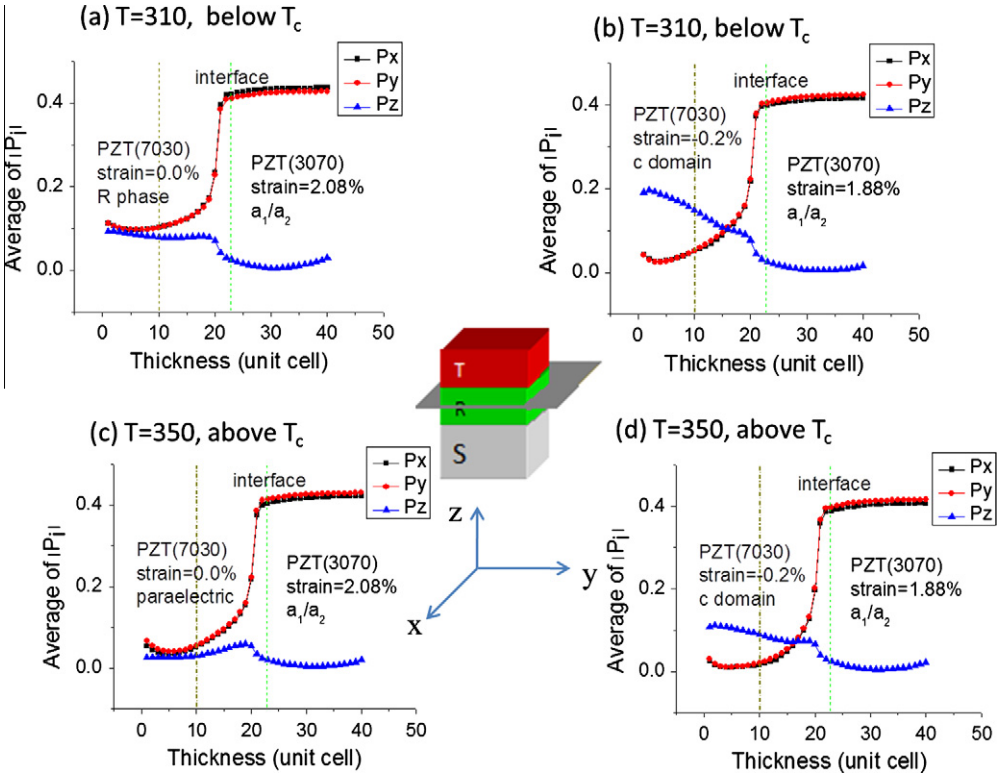

Fig. 7. Average polarization along the thickness direction (a) at 310 °C and under tensile substrate strain 1.04%; (b) at 310 °C and under tensile substrate strain 0.84%; (c) at 350 °C and under tensile substrate strain 1.04%; (d) at 350 °C and under tensile substrate strain 0.84%. The strain noted in the figure refers to effective in-plane strain in each separate layer.

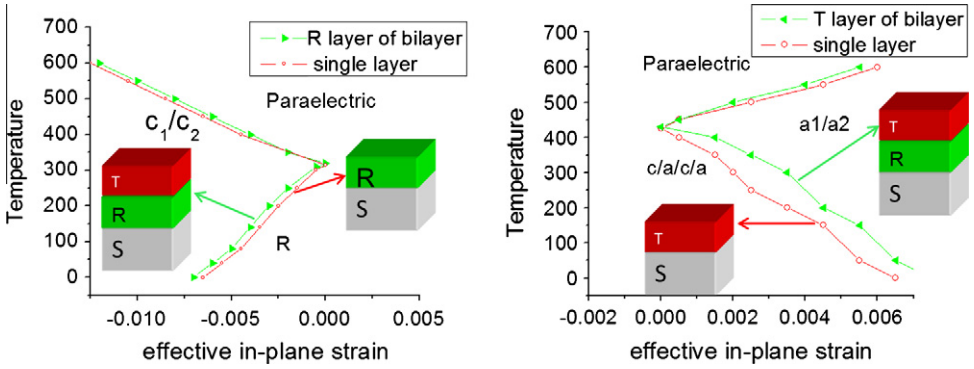

Fig. 8. Phase diagrams of a bi-layer and a single layer. The left figure shows phase diagrams of the R layer of a bi-layer (green line with triangles) and a single R film (red line with circles); the right figure refers to phase diagrams of the T layer of a bi-layer (green line with triangles) and a single T film (red line with circles).

This is somehow contradictory to the conclusion using thermodynamic calculations, which showed that the phase boundaries of the bilayer are significantly different from that of the single layer [13]. The difference may be because in the thermodynamic calculations the difference in the substrate constraint strains of the bilayer and single layer films were not considered, i.e. it was assumed that the two layers have the same lattice parameters. In that model the strains in both layers are equal to the substrate strain, which cannot be true since the lattice parameters of the two layers are quite different.

7. Conclusion

A three-dimensional phase field model was employed to study ferroelectric bilayer domain structures. It was demonstrated that at room temperature (much lower than the Curie temperatures) the misfit strain caused by the lattice parameter differences between the two layers leads to domain structures significantly different from that of the single layer. The domain sizes in the rhombohedral bilayer are reduced compared with the single layer case under the effect of a tetragonal layer. Above the Curie temperature

of the rhombohedral layer the bilayer shows a "ferroelectric proximity" effect resulting in induced polarization in the paraelectric layer. Therefore, not only can the bottom layer serve as the controlling interface for the top layer, but also the electrostatic and elastic interactions between the two layers can lead to certain domain structures uncommon in a single layer film. These domain structures may be sensitive to external electric fields, resulting in pronounced electromechanical properties. It is thus shown that designing a bilayer structure is a powerful method for tuning domain structures and their related physical properties.

Acknowledgements

This work was supported by the NSF MRSEC under Grants Nos. DMR-0820404, DMR-1006541, and DMR-1210588. The work at UNSW was supported by the ARC Discovery Project scheme.

References

[1] Dawber M, Stucki N, Lichtensteiger C, Gariglio S, Ghosez P, Triscone J-M. Adv Mater 2007;19:4153.
[2] Zhong S, Alpay SP, Cole MW, Ngo E, Hirsch S, Demaree JD. Appl Phys Lett 2007;90:092901.
[3] Boldyreva K, Pintilie L, Lotnyk A, Misirlioglu IB, Alexe M, Hesse D. Appl Phys Lett 2007;91:122915.
[4] Lee HN, Christen HM, Chisholm MF, Rouleau CM, Lowndes DH. Nature 2005;433:395.
[5] Pontes FM, Longo E, Leite ER, Varela JA. Appl Phys Lett 2004;84:5470.
[6] Vrejoiu I, Zhu YL, Le Rhun G, Schubert MA, Hesse D, Alexe M. Appl Phys Lett 2007;90:072909.
[7] Wang C, Fang QF, Zhu ZG, Jiang AQ, Wang SY, Cheng BL, et al. Appl Phys Lett 2003;82:2880.
[8] Zhou ZH, Xue JM, Li WZ, Wang J, Zhu H, Miao JM. J Appl Phys 2004;96:5706.
[9] Bungaro C, Rabe KM. Phys Rev B 2004;69:184101.
[10] Tian W, Jiang JC, Pan XQ, Haeni JH, Li YL, Chen LQ, et al. Appl Phys Lett 2006;89:092905.
[11] Roytburd AL, Zhong S, Alpay SP. Appl Phys Lett 2005;87:092902.
[12] Anbusathaiah V, Kan D, Kartawidjaja FC, Mahjoub R, Arredondo MA, Wicks S, et al. Adv Mater 2009;21:3497.
[13] Mahjoub R, Alpay SP, Nagarajan V. Phys Rev Lett 2010;105:197601.
[14] Kartawidjaja FC, Sim CH, Wang J. J Appl Phys 2007;102:124102.
[15] Mahjoub R, Anbusathaiah V, Alpay SP, Nagarajan V. J Appl Phys 2008;104:124103.
[16] Artemev A, Geddes B, Slutsker J, Roytburd A. J Appl Phys 2008;103:074104.
[17] Wang YZ, Chen LQ. Methods in materials research. New York: John Wiley & Sons; 2000.
[18] Nambu S, Sagala DA. Phys Rev B 1994;50:5838.
[19] Hu HL, Chen LQ. J Am Ceram Soc 1998;81:492.
[20] Semenovskaya S, Khachaturyan AG. J Appl Phys 1998;83:5125.
[21] Slutsker J, Artemev A, Roytburd A. Phys Rev Lett 2008;100:087602.
[22] Li YL, Hu SY, Liu ZK, Chen LQ. Acta Mater 2002;50:395.
[23] Khachatu Ag, Shatalov GA. Sov Phys Jetp-USSR 1969;29:557.
[24] Khachaturyan AG. Theory of structural transformations in solids. New York: Wiley; 1983.
[25] Stroh AN. J Math Phys 1962;41:77.
[26] Ting TCT. Anisotropic elasticity: theory and applications. Oxford: Oxford University Press; 1996.
[27] Li YL, Choudhury S, Haeni JH, Biegalski MD, Vasudevarao A, Sharan A, et al. Phys Rev B 2006;73:184112.
[28] Zhang JX, Li YL, Choudhury S, Chen LQ, Chu YH, Zavaliche F, et al. J Appl Phys 2008;103:094111.
[29] Sheng G, Zhang JX, Li YL, Choudhury S, Jia QX, Liu ZK, et al. J Appl Phys 2008;104:054105.
[30] Li YL, Hu SY, Tenne D, Soukiassian A, Schlom DG, Xi XX, et al. Appl Phys Lett 2007;91:112914.
[31] Li YL, Hu SY, Tenne D, Soukiassian A, Schlom DG, Chen LQ, et al. Appl Phys Lett 2007;91:252904.
[32] Zhong WL, Wang YG, Zhang PL, Qu BD. Phys Rev B 1994;50:698.
[33] Pertsev NA, Zembilgotov AG, Tagantsev AK. Phys Rev Lett 1998;80:1988.
[34] Tagantsev AK. Ferroelectrics 1986;69:321.
[35] Tagantsev AK. Ferroelectrics 2008;375:19.
[36] Woo CH, Zheng Y. Appl Phys A Mater Sci Process 2008;91:59.
[37] Kittel C. Introduction to solid state physics. New York: Wiley; 1996.
[38] Li YL, Hu SY, Liu ZK, Chen LQ. Appl Phys Lett 2002;81:427.
[39] Chen LQ, Shen J. Comp Phys Commun 1998;108:147.
[40] Haun MJ, Furman E, Jang SJ, McKinstry HA, Cross LE. J Appl Phys 1987;62:3331.
[41] Haun MJ, Furman E, Jang SJ, Cross LE. Ferroelectrics 1989;99:13.
[42] Khaenamkaew P, Muensit S, Bdikin IK, Kholkin AL. Mater Chem Phys 2007;102:159.
[43] Haun MJ, Zhuang ZQ, Furman E, Jang SJ, Cross LE. Ferroelectrics 1989;99:45.
[44] Pertsev NA, Kukhar VG, Kohlstedt H, Waser R. Phys Rev B 2003;67:054107.
[45] Hu SY, Li YL, Chen LQ. J Appl Phys 2003;94:2542.
[46] Li YL, Hu SY, Choudhury S, Baskes MI, Saxena A, Lookman T, et al. J Appl Phys 2008;104:104110.
[47] Bastani Y, Bassiri-Gharb N. Acta Mater 2012;60:1346.
[48] Chew KH, Ishibashi Y, Shin FG, Chan HLW. J Phys Soc Jpn 2003;72:2364.
[49] Li YL, Choudhury S, Liu ZK, Chen LQ. Appl Phys Lett 2003;83:1608.